

Particle swarm optimization tuned controllers for capacitor voltage balancing and harmonic suppression in modular multilevel converters

Mbark Outazkrit¹, Faicel El aamri², Essaid Jaoide¹, Abdelhadi Radouane¹, Azeddine Mouhsen¹

¹Laboratory of Radiation-Matter and Instrumentation, Faculty of Science and Technology, Hassan First University, Settat, Morocco

²Laboratory of Materials, Energy and System Control, Hassan II University, Mohammadia, Morocco

Article Info

Article history:

Received Jun 14, 2024

Revised Jan 21, 2025

Accepted Mar 3, 2025

Keywords:

Circulating current controller
Individual balancing capacitor
Modular multilevel converter
Particle swarm optimization
Proportional-resonant

ABSTRACT

The modular multilevel converter (MMC) has become a highly attractive power converter topology for various applications due to its modularity and scalability. However, it faces significant challenges, such as capacitor voltage balancing and circulating current, which can lead to instability and high-power losses. While the sorting algorithm is commonly used to balance capacitor voltages, this paper uses an individual balancing control method as an alternative. Additionally, a proportional resonant controller is employed to suppress the second and fourth harmonics in the circulating current. This paper presents a method for tuning the parameters of both the circulating current controller and the individual balancing control using the particle swarm optimization (PSO) algorithm, which represents the main contribution of this work. The MMC system, connected to a grid with a low number of submodules, is modeled and evaluated using the PLECS and MATLAB/Simulink environments. The results demonstrate the effectiveness of the proposed PSO-based tuning method in improving the performance and stability of the MMC.

This is an open access article under the [CC BY-SA](https://creativecommons.org/licenses/by-sa/4.0/) license.



Corresponding Author:

Mbark Outazkrit

Laboratory of Radiation-Matter and Instrumentation, Faculty of Science and Technology, University
Hassan First

Settat, Morocco

Email: m.outazkrit@uhp.ac.ma

1. INTRODUCTION

The modular multilevel converter (MMC) is a vital technology in high-voltage industries due to its scalability, high efficiency, and superior harmonic performance [1]. MMCs are widely used in medium and high-voltage applications, offering advantages like inherent fault tolerance [2], [3], low switching frequency [4], and excellent output waveform quality. Their modular structure allows for easy adjustments in voltage levels, making them suitable for a range of applications such as high voltage direct current (HVDC) transmission projects, medium-voltage motor drives, MMC photovoltaic system and static synchronous compensator (STATCOM) [5]–[7]. Despite their advantages, MMCs encounter significant challenges, particularly in capacitor voltage balancing and circulating current control. Failure to address these issues can result in system instability, increased energy losses, and a shortened lifespan of critical components, highlighting the necessity for advanced and effective control strategies [8].

To address the challenges associated with MMC, various research efforts have been undertaken. These efforts have explored different approaches, including innovative techniques inspired by natural processes and biological systems, such as particle swarm optimization (PSO) and genetic algorithms (GAs), used to find

optimal solutions for complex problems in MMC control. Lin *et al.* [9] have proposed a multi-objective optimization model using a genetic algorithm for reducing submodule (SM) capacitor voltage ripple and arm current root mean square (RMS) in modular multilevel converters. In [10], [11] presents a PSO algorithm-assisted modulation method to calculate improved selective harmonic elimination pulse width modulation (iSHE-PWM) switching angles, aiming to reduce total harmonic distortion (THD).

Another optimization strategy involves applying a fractional order proportional-integral-derivative (FOPID) controller to minimize circulating currents, with its parameters optimized using the wild spider foraging optimization (WSFO) algorithm [12]. Moreover, reference [13] combines PSO with bacterial chemotaxis to optimize proportional-resonance (PR) parameters for suppressing circulating currents. These optimization strategies demonstrate the potential of combining classical control methods with bio-inspired algorithms to enhance performance, stability, and efficiency in MMC systems.

Building on these advancements, this paper proposes the use of the PSO algorithm, chosen for its simplicity and ease of implementation. The proposed approach simultaneously tunes the parameters of the circulating current controller and the individual balancing controller, representing a novel dual-tuning strategy. Specifically, two PR controllers are optimized to suppress the second and fourth harmonics, reducing capacitor voltage fluctuations. A proportional controller is also tuned for the individual balancing controller to prevent capacitor voltage deviations, which could lead to converter instability.

Compared to article [12], which optimizes a FOPID controller using WSFO for circulating current control, and article [13], which focuses on a single PR controller for second harmonic suppression, both approaches optimize only the circulating current controller parameters. In contrast, the proposed method concurrently optimizes the parameters of both the circulating current controller and the individual balancing controller. This dual-optimization strategy delivers superior performance and improve system stability.

In section 2, the MMC system is described, followed by the presentation of the mathematical model. Section 3 details the control structure of the MMC, including the implementation of the PSO algorithm. Section 4 discusses simulation results that verify the performance of the converter with the parameters optimized by the algorithm. Finally, the conclusion is presented in section 5.

2. SYSTEM OVERVIEW AND MATHEMATICAL MODELING

A three-phase MMC used as an inverter is depicted in Figure 1. As shown, the three phases are connected to an AC grid through an inductor L_g and a resistor R_g . Each phase of the MMC consists of two arms, known as the upper and lower arms. An arm is formed by a series connection of N submodules, an arm inductor L , and an equivalent arm resistor R . The topology of the half-bridge submodule, illustrated in Figure 1, includes a capacitor (C) and two IGBTs with their antiparallel diodes ($D1$ and $D2$).

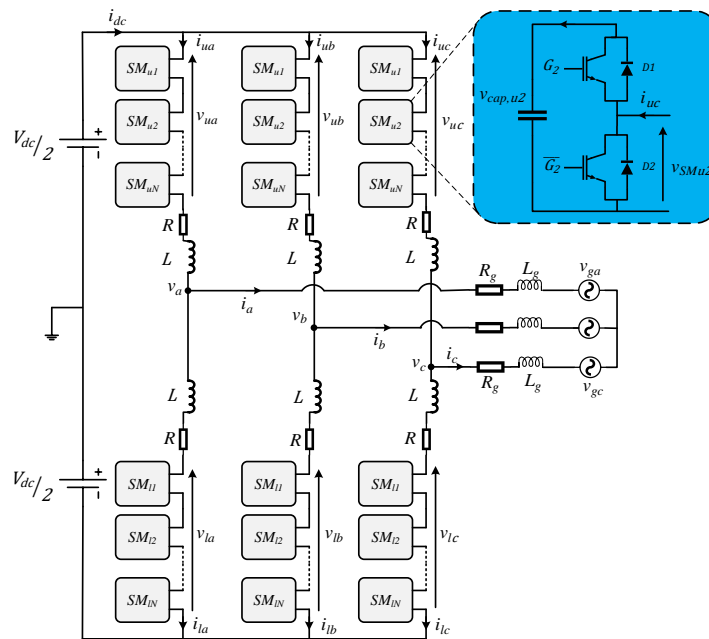


Figure 1. MMC connected to a grid with half-bridge submodule topology

Each arm can be considered as a variable voltage source controlled by an insertion index n , which is assumed to be a continuous variable [14]. When $n = 0$, it indicates that all N submodules in the arm are bypassed. Conversely, $n = 1$ indicates that all N submodules are inserted, meaning the arm current will circulate through all capacitors connected in series. The arm voltages can thus be expressed as a function of the insertion index and the sum of all capacitor voltages in the arm, as given by (1)

$$\begin{aligned} v_{uj} &= n_{uj} v_{cu_j}^\Sigma \\ v_{lj} &= n_{lj} v_{cl_j}^\Sigma \end{aligned} \quad (1)$$

where $j = a, b$ and c illustrate the three phases. v_{uj} and v_{lj} are the SM arm voltages. The variation of the sum capacitor voltages due to the arm current is given by (2).

$$\begin{aligned} \frac{C}{N} \frac{dv_{cu_j}^\Sigma}{dt} &= n_{uj} i_{uj} \\ \frac{C}{N} \frac{dv_{cl_j}^\Sigma}{dt} &= n_{lj} i_{lj} \end{aligned} \quad (2)$$

The dynamics of these voltages are affected by the arm current, particularly by the presence of harmonics in the circulating current [15]. The mathematical models of upper and lower arms are expressed as in (3) and (4).

$$v_{uj} = n_{uj} v_{cu_j}^\Sigma = \frac{V_{dc}}{2} - v_j - R i_{uj} - L \frac{di_{uj}}{dt} \quad (3)$$

$$v_{lj} = n_{lj} v_{cl_j}^\Sigma = \frac{V_{dc}}{2} + v_j - R i_{lj} - L \frac{di_{lj}}{dt} \quad (4)$$

where R and L specify the arm resistance and arm inductance, respectively. V_{dc} denotes the DC link voltage and v_j denotes the output voltage. Different currents of MMC are written as (5) and (6).

$$i_j = i_{uj} - i_{lj} \quad (5)$$

$$i_{circj} = \frac{i_{uj} + i_{lj}}{2} \quad (6)$$

The circulating current and output current are expressed in terms of upper and lower arm currents as in (7) and (8).

$$i_{uj} = \frac{i_j}{2} + i_{circj} \quad (7)$$

$$i_{lj} = -\frac{i_j}{2} + i_{circj} \quad (8)$$

where i_{lj} , i_{uj} , and i_j represent lower arm current, upper arm current, and output current, respectively. i_{circj} denotes the circulating current. From (3) and (4) we can demonstrate that the circulating current is controlled by the average voltage of the upper and lower arms v_{sumj} as defined in the (8) and (9):

$$\begin{aligned} v_{diffj} &= \frac{V_{dc}}{2} - v_{sumj} = R i_{circj} + L \frac{di_{circj}}{dt} \\ v_{sumj} &= \frac{v_{uj} + v_{lj}}{2} = \frac{n_{uj} v_{cu_j}^\Sigma + n_{lj} v_{cl_j}^\Sigma}{2} \end{aligned} \quad (9)$$

v_{diffj} represents the unbalance voltage of phase j . The output voltage of the converter v_j is determined by rearranging (3)-(5):

$$v_j = e_j - \frac{R}{2} i_j - \frac{L}{2} \frac{di_j}{dt} \quad (10)$$

Here, e_j represent the driving voltage of output current i_j is expressed as (11)

$$e_j = \frac{v_{lj} - v_{uj}}{2} = \frac{n_{lj} v_{cl_j}^\Sigma - n_{uj} v_{cu_j}^\Sigma}{2} \quad (11)$$

3. CONTROL ARCHITECTURE OF MMC

The control architecture of the MMC includes three primary stages: the output current controller, the circulating current controller, and the capacitor voltage balancing controller. These stages work in coordination to ensure stable operation, harmonic suppression, and voltage balancing. Figure 2 provides an overview of the control structure, highlighting the interdependence of these components.

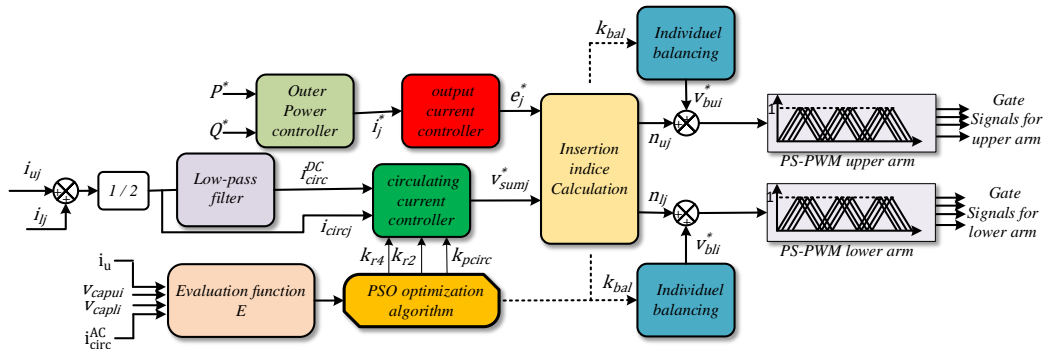


Figure 2. Overall MMC control structure

3.1. Output current controller

The output current controller is designed to ensure that the MMC generates sinusoidal output currents with minimal distortion. To achieve this, a PR controller is employed, tuned specifically to the grid frequency for optimal performance. Consequently, this approach helps meet the reactive power or power factor requirements of the system, which is essential for ensuring efficient power transfer, reducing power losses, and maintaining overall stability and reliability in grid-connected applications.

Figure 3(a) shows the equivalent model of the three-phase MMC for output current deduced from (10) and (11). The expression of output current is expressed as (12).

$$i_j(s) = \frac{1}{s \cdot (\frac{L}{2} + L_g) + \frac{R}{2} + R_g} (e_j - v_{gj}) \tag{12}$$

The output current reference denoted as i_j^* is derived from the active and reactive power references. To accurately track this reference current, which follows a fundamental-frequency sinusoid, the PR controller shown in Figure 3(b) is used. Its resonant part is tuned to the grid frequency, making it an appropriate choice for this application.

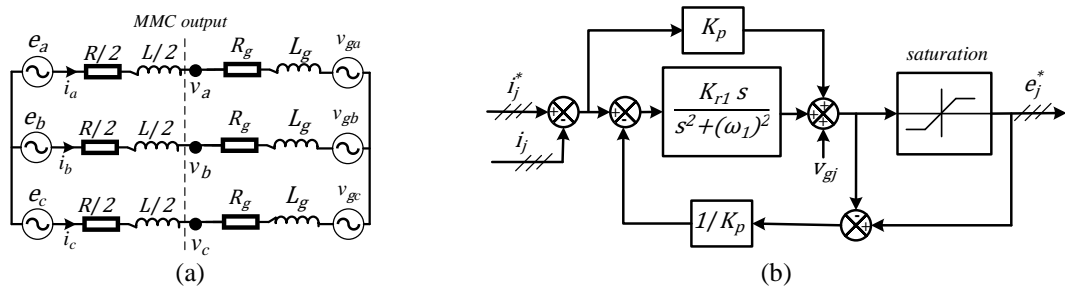


Figure 3. Output current: (a) equivalent model and (b) block representation of the controller [16]

The proportional gain K_p is calculated based on the closed-loop bandwidth α_c , as well as the grid and arm inductance, as shown (13).

$$K_p = \alpha_c \cdot (\frac{L}{2} + L_g) \tag{13}$$

The bandwidth is selected based on the number of submodules N and the carrier frequency f_c . Its value must be chosen as (14).

$$\alpha_c \leq \frac{4\pi N \cdot f_c}{10} \tag{14}$$

The resonant gain K_{r1} is determined by the (15).

$$K_{r1} = 2 \cdot \alpha_1 \cdot K_p \tag{15}$$

where α_1 , is the resonant bandwidth, which must be less than the angular frequency $\alpha_1 < \omega_1$ [16].

3.2. Circulating current controller

Another crucial control stage is the circulating current controller, which helps reduce the RMS value of the arm currents and minimizes voltage ripples in the submodule (SM) capacitors [17]. The control objective is to suppress the second and fourth harmonics, the dominant components in this current. The circulating current components can be expressed as (16) [18]:

$$i_{circj}(t) = i_{circDC} + i_{circAC}(t) = \frac{i_{dc}}{3} + I_{2max} \sin(2\omega_1 t + \theta_2) + I_{4max} \sin(4\omega_1 t + \theta_4) \tag{16}$$

where $i_{dc}/3$ is the DC component of the circulating current, and I_{2max} and I_{4max} are the maximum values of the second and fourth order harmonic components of the circulating current, and θ_2 and θ_4 are their corresponding phase angles.

To suppress these undesirable components, two control methods are proposed in this paper. The first method employs a PR controller, while the second uses only a Proportional (P) controller. The block diagram of circulating current controller is illustrated in Figure 4.

In the first method, as depicted in Figure 4(a), the AC components $i_{circj}^{AC}(t)$ are extracted by subtracting the DC component i_{circj}^{DC} (obtained using a low-pass filter) from the total circulating current $i_{circj}(t)$. The objective is to eliminate the AC components $i_{circj}^{AC}(t)$, so the reference value is set to zero, effectively suppressing the unwanted oscillations. To achieve this, two PR controllers are used, each specifically tuned to frequencies of 100 and 200 Hz, respectively [19]. The transfer function of the PR controllers is defined as (17).

$$G_{PR}(s) = K_{pcirc} + \frac{K_{r2} \cdot s}{s^2 + (2\omega_1)^2} + \frac{K_{r4} \cdot s}{s^2 + (4\omega_1)^2} \tag{17}$$

The second method employs a simple Proportional controller (K_1) in combination with a moving average filter (MAF) to extract the AC component $i_{circj}^{AC}(t)$ of the circulating current $i_{circj}(t)$. The control scheme for this method is illustrated in Figure 4(b) [20], [21]. Like the first method, the controller's reference is set to zero to suppress the AC components effectively.

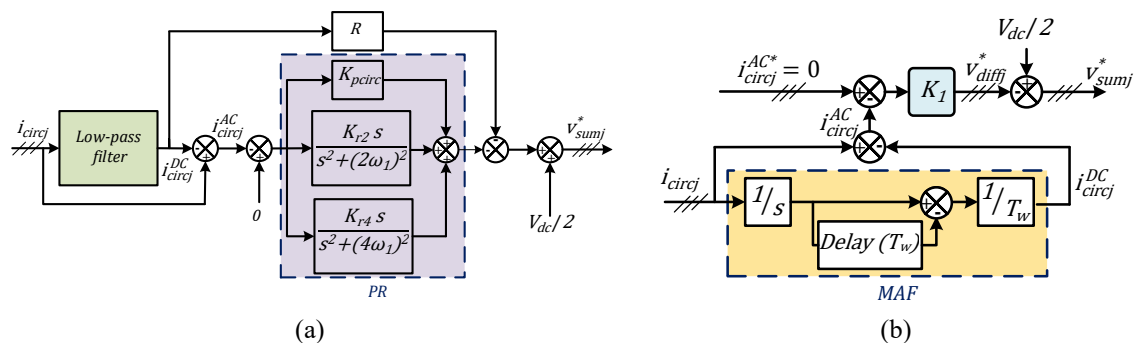


Figure 4. Block representation of the circulating current controller: (a) method 1, (b) method 2

To separate the AC and DC components in the circulating current, the MAF is designed with a frequency equal to twice the grid frequency ($f_w = 1/T_w = 2f_1$), where T_w represents the window width of the

MAF. However, there is no explicit mathematical formula to determine the value of K_1 ; its selection is typically based on system performance and tuning considerations. For the first control method, the parameters K_{pcirc} , K_{r2} and K_{r4} must be properly selected to ensure optimal performance of the converter. These parameters are calculated using the (18), emphasizing the importance of precise tuning to achieve satisfactory control dynamics and overall stability of the system.

$$\begin{aligned}
 R &\ll K_{pcirc} \leq K_p \\
 K_{r2} &= 2 \cdot \alpha_2 \cdot K_{pcirc} \\
 K_{r4} &= 2 \cdot \alpha_4 \cdot K_{pcirc}
 \end{aligned}
 \tag{18}$$

The parameter K_{pcirc} must not exceed K_p , the proportional gain of the output current. Additionally, the resonant bandwidths α_2 and α_4 should be less than the grid's angular frequency ω_1 [16]. Various gain choices can be derived from this equation; however, they are typically tested using the trial-and-error method. To overcome the limitations of manual tuning and enhance tracking performance, a PSO algorithm is employed to fine-tune the parameters of the circulating current controller for both the first and second methods.

3.3. Insertion indices calculation

The insertion indices n_{uj} and n_{lj} can be used to determine the number of submodules inserted into each arm. These indices are calculated based on the output current and circulating current references as given by (19). The indices directly affect the voltage generated by each arm, ensuring proper balancing [22]. Gate signals are then generated by comparing the sum of the insertion indices with the output of the individual balancing controller and phase-shift pulse width modulation (PWM) carriers.

$$\begin{aligned}
 n_{uj} &= \frac{v_{sumj}^* - e_j^*}{V_{dc}} \\
 n_{lj} &= \frac{v_{sumj}^* + e_j^*}{V_{dc}}
 \end{aligned}
 \tag{19}$$

3.4. Individual balancing controller

Capacitor voltage balancing is one of the most important control objectives. When it is not ensured, it can lead to system instability. The primary objective of this controller is to maintain the capacitor voltage of each submodule at its reference value $v_c^* = V_{dc}/N$. In this paper, we use an individual balancing controller, as depicted in Figure 5, instead of a sorting algorithm due to the low number of submodules in each arm [23]. This control is separately applied to every submodule, ensuring that each capacitor voltage is independently regulated.

The principle of individual balancing controller is to compare each measured capacitor voltage v_{capui} with the reference voltage v_c^* , and the error is fed to a proportional controller K_{bal} to minimize this error. The reference v_{bui}^* is obtained when the output of the proportional controller is multiplied by the direction of the arm current [24], [25]. To implement such individual voltage control, a phase-shifted PWM modulation scheme is required. However, tuning K_{bal} traditionally involves a trial-and-error approach, and its value must remain much less than 1 to prevent disturbances in the insertion indices. Therefore, the PSO algorithm is used to optimize the gain value of this controller and prevent capacitor voltage divergence.

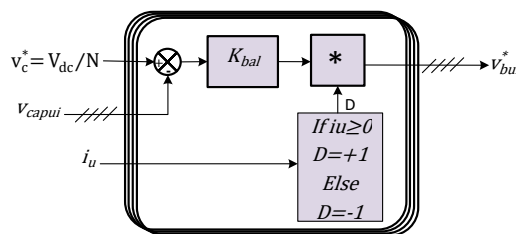


Figure 5. Individual balancing controller for upper arm

3.5. Description of PSO algorithm

In this paper, the PSO algorithm has been utilized for an optimal tuning of the circulating current and individual balancing controller's parameters. PSO is an efficient heuristic search method that uses M particles dispersed in a D-dimensional research space to find the global minimum of an objective function. The basic

principle of PSO is inspired by the social behavior of animals moving in swarm [26]. The PSO algorithm systematically adjusts the controller gains K_{pcirc} , K_{r2} , K_{r1} and K_{bal} for control method 1, as well as K_1 and K_{bal} for control method 2. To ensure effective optimization, a suitable evaluation function as outlined in [27] is required. Each particle i has a position vector $X_i(t)$ and a velocity vector $V_i(t)$, where t is the iteration counter. In the D -dimensional search space, the position vector $X_i(t)$ and the velocity vector $V_i(t)$ of the i th particle can be represented as $X_i = (X_{i1}, X_{i2}, \dots, X_{iD})$ and $V_i = (V_{i1}, V_{i2}, \dots, V_{iD})$, respectively.

The movements of particles in the search space are evaluated using a predefined evaluation function. During each iteration, each particle retains a memory of the best position it has discovered so far, known as its personal best value P_{best} . Meanwhile, the particle with the best P_{best} in the total swarm is called the global best particle G_{best} .

Then, the next position vector $X_i(t + 1)$ and velocity vector $V_i(t + 1)$, of the particles are calculated via P_{best} , G_{best} , $X_i(t)$, and $V_i(t)$. The updated equations are derived as (20) and (21).

$$V_i(t) = \omega \times V_i(t - 1) + c_1 \times rand_1 \times (P_{best}(t) - X_i(t)) + c_2 \times rand_2 \times (G_{best}(t) - X_i(t)) \quad (20)$$

$$X_i(t + 1) = X_i(t) + V_i(t + 1) \quad (21)$$

where $rand_1$ and $rand_2$ are two random numbers uniformly distributed in the interval $[0,1]$; c_1 and c_2 are the acceleration constants, and ω is the inertia weight factor [11].

Next, the evaluation function E is selected based on three terms. The first one is the THD of the arm current in the steady state, ideally zero when there are no harmonics in the circulating current. The second term is the integral time absolute error (ITAE) of the difference between the reference zero and the AC components of the circulating current. The final term reflects the deviation of capacitor voltages. This function is represented by the (22).

$$E = |0 - THD_{iarm}| + \int_0^\infty t \cdot |0 - i_{circ}^{AC}| dt + \frac{|\sum_{i=1}^N |v_{capui} - \langle v_{capui} \rangle| - \sum_{i=1}^N |v_{capli} - \langle v_{capli} \rangle|}{N} \quad (22)$$

The flowchart in Figure 6 depicts the implementation of the PSO algorithm for parameter estimation of the proposed controllers. The specific values assigned to the PSO algorithm parameters used in this study are provided in Table 1. As shown, the search space dimension D varies between 4 for method 1 and 2 for method 2, indicating a difference in the complexity of the optimization problem for each method. Additionally, the algorithm employs a population of 20 particles and is executed for a maximum of 15 iterations, ensuring a reasonable trade-off between computational efficiency and accuracy.

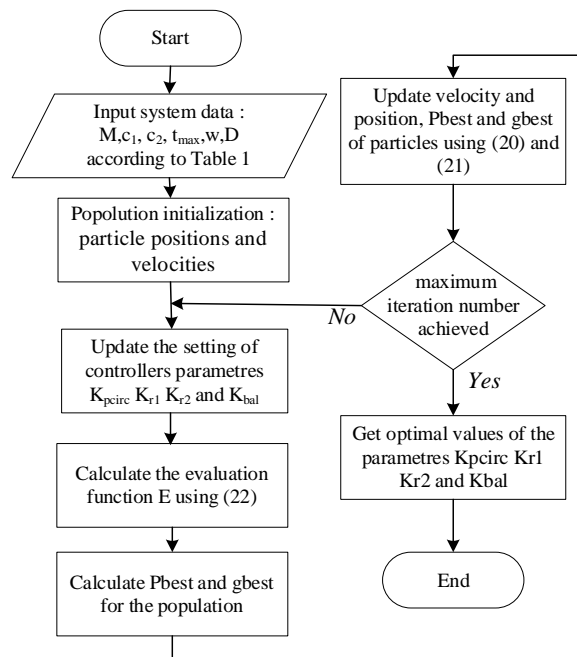


Figure 6. Flowchart for PSO algorithm

Table 1. The parameters values of the PSO algorithm

Parameter	Value
Search space dimension D	4 (method 1)/ 2 (method 2)
Maximum number of iterations t_{max}	15
Number of particles M	20
c1	2
c2	2
Inertia weight w	0.9

4. RESULTS AND DISCUSSION

This section presents and analyzes the simulation results to validate the effectiveness of the controller gains optimized using the PSO algorithm for both control methods. The simulations were conducted using MATLAB/Simulink and PLECS for a three-phase MMC-based inverter connected to the grid. The key parameters employed in the simulations are provided in Table 2. These simulations aim to evaluate and compare the performance of the optimized controllers for both methods in terms of capacitor voltage balancing, minimization of capacitor voltage ripples, and suppression of circulating currents.

Table 2. System parameters

Parameters	Value
DC link-voltage V_{DC}	10000 V
Peak output current I_{max}	200 A
Grid peak voltage	4750 V
Grid inductance L_g	8 mH
Grid resistance R_g	0.25 Ω
Arm inductance L	12 mH
Arm resistance R	0.4 Ω
Number of SMs per arm N	4
Nominal SM voltage	2500 V
Submodule capacitance C	0.6 mF
Grid frequency f_{grid}	50 Hz
Carrier frequency f_c	2000 Hz
Proportional gain of the output current K_p	68.4
Resonant gain of the output current K_{r1}	6840
Rated power factor	1

The performance of the PSO algorithm is evaluated by plotting the convergence of the evaluation function E over successive iterations, as shown in Figure 7. The function E decreases progressively with an increasing number of iterations, reflecting the optimization process. Due to the computational cost of PSO, the simulations were limited to 15 iterations. Furthermore, the combination of MATLAB and PLECS increases the simulation time for each iteration. At the end of simulation, the optimized parameter values for both methods are summarized in Table 3.

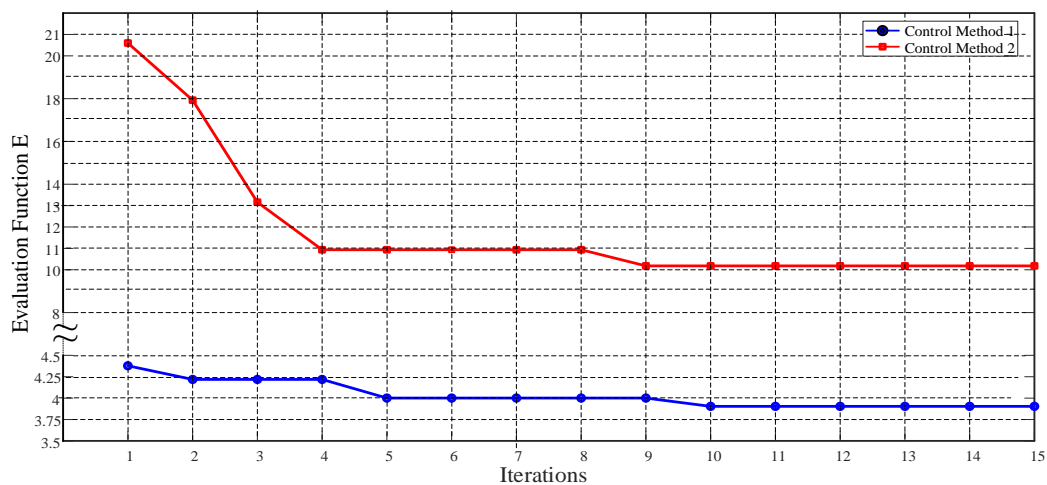


Figure 7. The evolution function at each iteration for both control methods

Table 3. Circulating current and balancing controller parameters optimized with PSO

$K_{p\text{circ}}$	Control method 1			E	Control method 2		
	K_{r2}	K_{r4}	K_{bal}		K_1	K_{bal}	E
33.47	87.12	261.2	$2.407 \cdot 10^{-5}$	3.904	46.18	$9.3 \cdot 10^{-7}$	10.182

For comparison purposes, both methods utilize the same evaluation function E . The results reveal that control Method 1 achieves a lower value of the evaluation function ($E = 3.904$) compared to control method 2 ($E = 10.182$), indicating superior performance in terms of circulating current suppression and capacitor voltage balancing. This improvement can be attributed to the effectiveness of the PR controllers in suppressing circulating currents, which outperforms the simpler proportional controller used in control method 2.

To evaluate the effectiveness of the PSO tuning methodology in addressing key MMC challenges such as circulating current suppression and capacitor voltage ripple reduction, several simulations were conducted. Figure 8 illustrates the output waveforms for all three phases. Both control methods produce similar current and voltage waveforms, demonstrating the successful tuning achieved by the PSO algorithm and the stable operation of the MMC. Specifically, Figure 8(a) depicts the output currents in each phase, which are nearly ideal sinusoidal waveforms with a low THD of 0.7% and amplitudes of approximately 200 A. This reflects the accuracy of the output current controller.

The output voltages for both methods consist of multiple voltage steps, as illustrated in Figure 8(b), with each phase exhibiting nine distinct levels. The THD of these voltages is approximately 10.7%, attributed to the presence of ripples in the capacitor voltages. In comparison, article [12] reports a THD of 7.58% using a PSO-FOPID controller combined with a sorting algorithm. This difference can be explained by the superior ability of the sorting algorithm to balance capacitor voltages compared to the individual balancing method used in this paper, as well as the influence of the load characteristics.

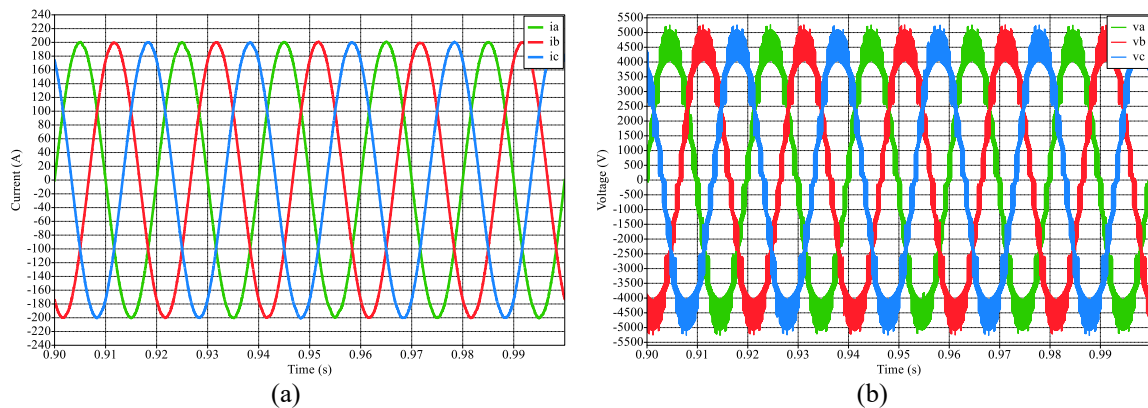


Figure 8. Output waveforms: (a) output currents and (b) output voltages

In order to further verify the suppression capacity of the optimized CCC for both control methods, we assumed that the individual balancing controller is activated at $t = 0$ s and the CCC is put into operation at 0.5 s. Before the controller is activated, significant oscillations are observed in i_{circa} for both methods which are explained by the presence of several harmonics. After activation, the circulating current i_{circa} of control method 1 rapidly converges towards the reference $i_{\text{circ_DC}}$ after a rush transition phase, demonstrating effective suppression of oscillations. In contrast, control method 2 shows slower convergence and more pronounced residual oscillations as illustrated in Figure 9.

The harmonic spectra of i_{circa} for both control methods are depicted in Figure 10, showing the results before and after the activation of the optimized CCC. Figure 10(a) illustrates the harmonic composition of i_{circa} before the activation. Both methods exhibit the same DC component, approximately 48.5 A, which closely matches the reference value of $i_{\text{circ_DC}} = 47.5$ A. However, higher-order harmonics are also prominent, contributing to circulating current oscillations. Specifically, the 100 Hz harmonic reaches 92.7 A for-control method 2 and 95.7 A for-control method 1, while the 200 Hz harmonic amplitudes are 3.4 A and 6.5 A for-control method 2 and control method 1, respectively. These harmonics are the primary cause of the oscillations observed in Figure 9 before the activation of the CCC.

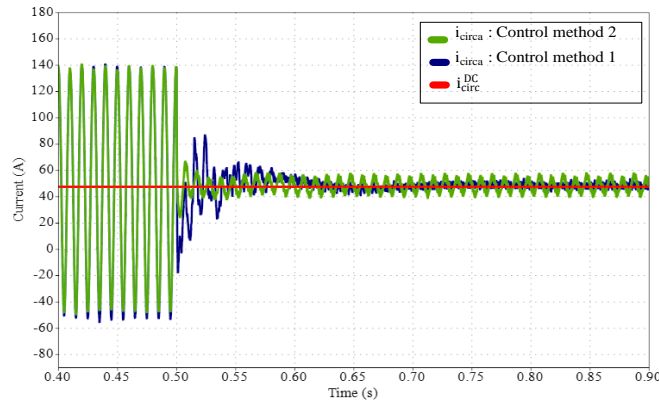


Figure 9. Circulating current in phase A for both control methods

Once the CCC is activated, significant improvements in harmonic suppression are observed. control method 1, which utilizes two PR controllers tuned with the PSO algorithm, achieves superior suppression of both the second and fourth harmonics, as demonstrated in Figure 10(b). In comparison, control method 2, which employs a single P controller also tuned with the PSO algorithm, effectively suppresses the fourth harmonic and reduces the second harmonic to 6.12 A. These results highlight the overall effectiveness of the PSO algorithm in determining the optimal controller gains for both methods.

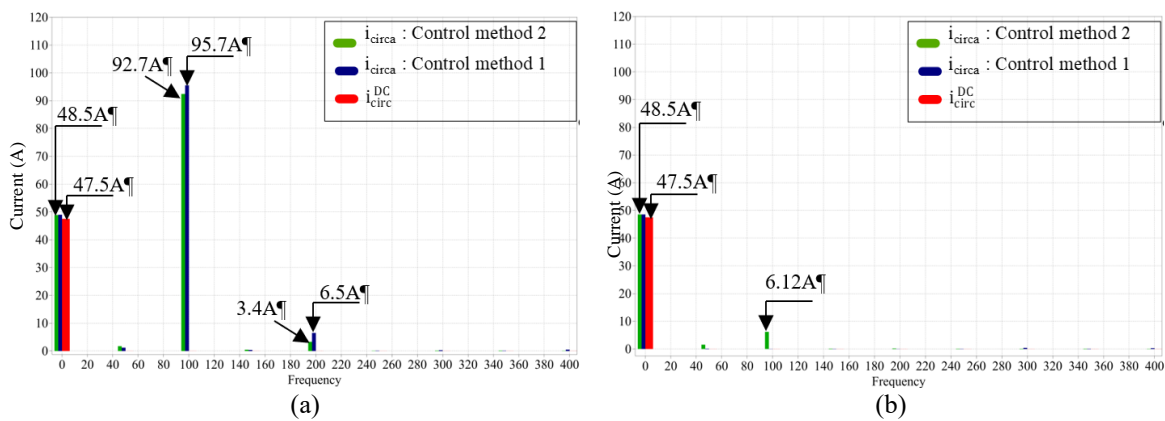


Figure 10. Harmonic spectra of i_{circa} : (a) before activating the CCC and (b) after activating the CCC

Circulating current significantly impacts the shape of arm currents, as illustrated in Figure 11. Before the activation of the CCC, the arm current i_{ua} is noticeably deformed due to the presence of second and fourth harmonics, resulting in fluctuations ranging from approximately -154 to 164 A. These distortions increase the RMS and peak values of the arm currents, potentially affecting component ratings and system efficiency. After the CCC is activated, i_{ua} becomes nearly sinusoidal, with reduced fluctuations ranging from -56 to 150 A. However, slight variations persist due to high harmonics introduced by the modulation scheme.

The harmonic composition of i_{ua} for both control methods is shown in Figure 12. The current i_{ua} contains the same harmonic components as i_{circa} , with an additional harmonic at 50 Hz, representing half of the output current, as explained by (7) and (8). This harmonic has a magnitude of approximately 100 A, as depicted in Figure 12(a). After the activation of the optimized CCC, control method 1 achieved superior suppression of the second and fourth harmonics, resulting in a THD of 2.2%. Meanwhile, control method 2 effectively suppressed the second harmonic and reduced the fourth harmonic, achieving a THD of 6.12%, as depicted in Figure 12(b). These results highlight the effectiveness of the parameters optimized by the PSO algorithm in minimizing circulating current and improving arm current quality for both control methods.

Figure 13 illustrates the arm voltage v_{ua} and the sum of capacitor voltages v_{cua}^{Σ} for both control methods. The arm voltages v_{ua} have six levels ($N + 1$), ideally varying from zero to the DC-link voltage V_{DC} .

Before the activation of the CCC, the arm voltage v_{ua} exceeds V_{DC} , reaching a maximum value of 1.17 kV. The total capacitor voltages v_{cua}^{Σ} display a peak-to-peak voltage ripple of approximately $v_{ppu} = 3448 V$ for control method 1 and $v_{ppu} = 3442V$ for control method 2, as illustrated in Figures 13(a) and 13(b).

After the activation of the optimized CCC, the peak-to-peak voltage ripple is significantly reduced to $v_{ppu} = 1448 V$ for control method 1 and $v_{ppu} = 1503 V$ for control method 2. This reduction highlights the improved individual balancing achieved through the optimization provided by the PSO algorithm. The remaining difference in ripple between the two methods can be attributed to the presence of the fourth harmonic in the arm current, which causes greater fluctuations in v_{cua}^{Σ} for the control method 2.

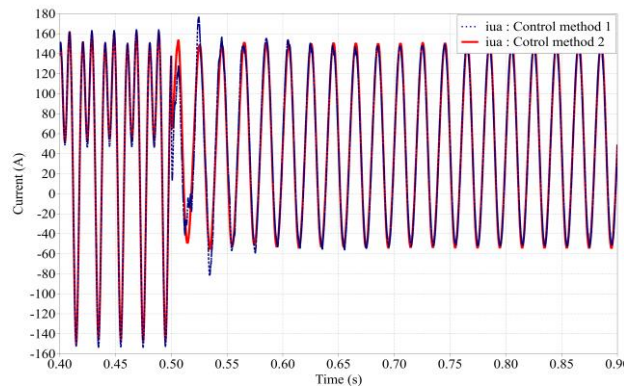


Figure 11. Arm currents in phase A

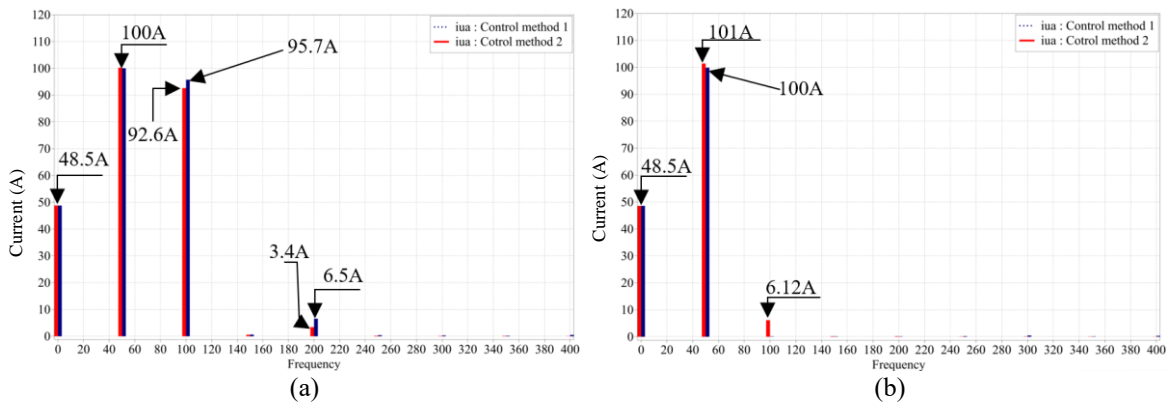


Figure 12. Harmonic spectra of i_{ua} : (a) before activating the CCC and (b) after activating the CCC

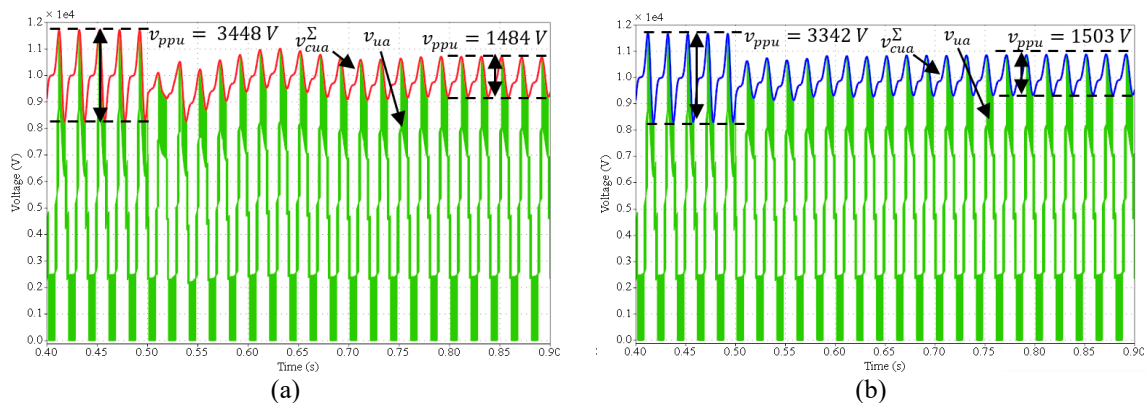


Figure 13. Arm voltage and sum of capacitor voltages: (a) control method 1 and (b) control method 2

Figure 14 illustrates the capacitor voltages in the upper arm of phase A for both control methods. Before activating the CCC, only the individual balancing controller, based on the proportional controller K_{bal} , is active. The gain K_{bal} is optimized using the PSO algorithm for both control methods. As shown in Figures 14(a) and 14(b), all capacitor voltages within the same arm are balanced, exhibiting identical waveforms and following the same pattern. Each capacitor voltage oscillates around its reference value ($v_c^* = 2500\text{ V}$). The only difference lies in the voltage ripple (v_{ppu}), which is 862 V ($K_{bal} = 2.407 \cdot 10^{-5}$) for control method 1 and 840 V ($K_{bal} = 9.3 \cdot 10^{-7}$) for control method 2. These results demonstrate that the K_{bal} gains, tuned using the PSO algorithm, effectively balance the individual capacitor voltages.

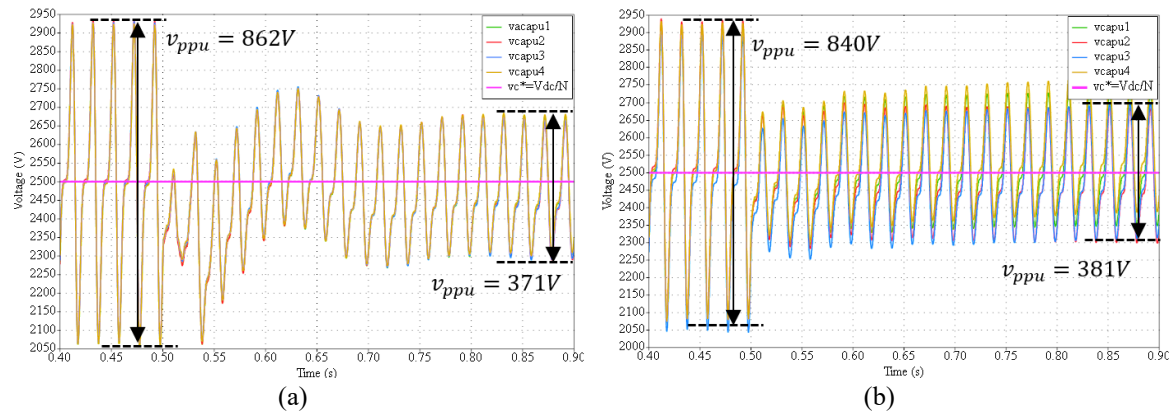


Figure 14. Waveforms of SM capacitor voltages in upper arm: (a) control method 1 and (b) control method 2

After activating the optimized CCC, the capacitor voltage ripple is significantly reduced to $v_{ppu} = 371\text{ V}$ for control method 1, with the waveform shape remaining consistent across all capacitors. In contrast, for control method 2, the ripple is reduced to $v_{ppu} = 381\text{ V}$, but slight dispersion in the capacitor voltages begins to appear. These results clearly demonstrate the critical role of circulating current controller in minimizing capacitor voltage ripple and maintaining voltage uniformity.

5. CONCLUSION

In this paper, PSO was applied to optimize the control of a MMC connected to a grid system operating in inverter mode. The PSO algorithm was used to simultaneously tune the gains of the circulating current and individual balancing voltage controllers, which represents the main contribution of this work. Two control methods were implemented for comparison purposes.

Control method 1 incorporates two PR controllers to suppress circulating current, specifically targeting the second and fourth harmonics, along with a proportional controller for the individual balancing of submodule capacitors. In total, this method optimizes four parameters ($K_{pcirc}, K_{r2}, K_{r4}$ and K_{bal}) using the PSO algorithm. On the other hand, control method 2 utilizes a simpler structure, with only two parameters (K_1 for the circulating current controller and K_{bal} for the individual balancing controller), which are also tuned using PSO.

Simulation results validated the effectiveness of the optimized parameters, demonstrating superior suppression of the second and fourth harmonics in control method 1, resulting in significantly reduced circulating current oscillations and improved arm current quality. The arm currents achieved quasi-sinusoidal waveforms with significantly reduced THD values. Furthermore, the individual balancing controller successfully maintained capacitor voltage stability, ensuring consistent voltage waveforms and reduced ripple values across all submodules. Both control methods minimized the peak-to-peak voltage ripples, with control method 1 showing better overall performance due to the enhanced capabilities of its PR controllers.

These achievements underscore the capability of PSO as a robust optimization technique, significantly enhancing the stability and performance of MMC systems. However, the PSO algorithm is sensitive to the configuration of its parameters, such as the initialization of particle positions and the definition of the objective function. Additionally, the algorithm incurs a high computational cost, particularly when a detailed submodule model is used in simulation. These limitations present interesting opportunities for future research, including the development of simplified submodule models to reduce computational cost, the exploration of alternative optimization algorithms, and the experimental validation of the proposed approach.

FUNDING INFORMATION

Authors state no funding involved.

AUTHOR CONTRIBUTIONS STATEMENT

This journal uses the Contributor Roles Taxonomy (CRediT) to recognize individual author contributions, reduce authorship disputes, and facilitate collaboration.

Name of Author	C	M	So	Va	Fo	I	R	D	O	E	Vi	Su	P	Fu
Mbark Outazkrit	✓	✓	✓	✓	✓	✓		✓	✓	✓				✓
Faichel El Aamri		✓				✓		✓	✓	✓	✓	✓	✓	
Essaid Jaouide	✓					✓			✓					
Abdelhadi Radouane					✓							✓	✓	
Azeddine Mouhsen					✓		✓			✓		✓		✓

C : **C**onceptualization

M : **M**ethodology

So : **S**oftware

Va : **V**alidation

Fo : **F**ormal analysis

I : **I**nterpretation

R : **R**esources

D : **D**ata Curation

O : **O**riginal Draft

E : **E**ditorial Review & **E**dit

Vi : **V**isualization

Su : **S**upervision

P : **P**roject administration

Fu : **F**unding acquisition

CONFLICT OF INTEREST STATEMENT

Authors state no conflict of interest.

INFORMED CONSENT

We have obtained informed consent from all individuals included in this study.

DATA AVAILABILITY

Data availability is not applicable to this paper as no new data were created or analyzed in this study.

REFERENCES

- [1] R. V. K. Challa, S. Mikkili, and P. K. Bonthagorla, "Modeling, controlling approaches, modulation schemes, and applications of modular multilevel converter: Review," *Journal of Control, Automation and Electrical Systems*, vol. 34, no. 1, pp. 189–215, Feb. 2023, doi: 10.1007/s40313-022-00953-8.
- [2] Q. Xiao *et al.*, "Review of fault diagnosis and fault-tolerant control methods of the modular multilevel converter under submodule failure," *IEEE Transactions on Power Electronics*, vol. 38, no. 10, pp. 12059–12077, Oct. 2023, doi: 10.1109/TPEL.2023.3283286.
- [3] M. N. Sakib, S. P. Azad, and M. Kazerani, "A critical review of modular multilevel converter configurations and submodule topologies from DC fault blocking and ride-through capabilities viewpoints for HVDC applications," *Energies*, vol. 15, no. 11, Jun. 2022, doi: 10.3390/en15114176.
- [4] Y. Luo, Z. Jia, L. Xu, Q. Li, and Y. Song, "A reduced switching frequency capacitor voltage balancing control for modular multilevel converters," *International Journal of Electrical Power & Energy Systems*, vol. 142, Nov. 2022, doi: 10.1016/j.ijepes.2022.108272.
- [5] A. Dekka, B. Wu, R. L. Fuentes, M. Perez, and N. R. Zargari, "Evolution of topologies, modeling, control schemes, and applications of modular multilevel converters," *IEEE Journal of Emerging and Selected Topics in Power Electronics*, vol. 5, no. 4, pp. 1631–1656, Dec. 2017, doi: 10.1109/JESTPE.2017.2742938.
- [6] H. Mei, C. Jia, J. Fu, and X. Luan, "Low voltage ride through control strategy for MMC photovoltaic system based on model predictive control," *International Journal of Electrical Power & Energy Systems*, vol. 125, Feb. 2021, doi: 10.1016/j.ijepes.2020.106530.
- [7] S. Zhou, B. Li, J. Wang, and D. Xu, "A modified modular multilevel converter for motor drives capable of high-torque operation at zero/low motor speeds," *IEEE Transactions on Circuits and Systems II: Express Briefs*, vol. 68, no. 7, pp. 2493–2497, Jul. 2021, doi: 10.1109/TCSII.2021.3058523.
- [8] M. A. Perez, S. Ceballos, G. Konstantinou, J. Pou, and R. P. Aguilera, "Modular multilevel converters: recent achievements and challenges," *IEEE Open Journal of the Industrial Electronics Society*, vol. 2, pp. 224–239, 2021, doi: 10.1109/OJIES.2021.3060791.
- [9] L. Lin, A. Li, C. Xu, and Y. Wang, "Multi-objective genetic algorithm based coordinated second- and third-order harmonic voltage injection in modular multilevel converter," *IEEE Access*, vol. 8, pp. 94318–94329, 2020, doi: 10.1109/ACCESS.2020.2995293.
- [10] X. Qin, W. Hu, Y. Tang, Q. Huang, Z. Chen, and F. Blaabjerg, "An improved modulation method for modular multilevel converters based on particle swarm optimization," *International Journal of Electrical Power & Energy Systems*, vol. 151, Sep. 2023, doi: 10.1016/j.ijepes.2023.109136.
- [11] Ke Shen *et al.*, "Elimination of harmonics in a modular multilevel converter using particle swarm optimization-based staircase modulation strategy," *IEEE Transactions on Industrial Electronics*, vol. 61, no. 10, pp. 5311–5322, Oct. 2014, doi: 10.1109/TIE.2013.2297301.

- [12] S. Balamurugan and S. Nageswari, "Circulating current control of modular multilevel converter by wild spider foraging optimization based fractional order proportional integral derivative controller," *Journal of Intelligent & Fuzzy Systems*, vol. 41, no. 2, pp. 4127–4147, Sep. 2021, doi: 10.3233/JIFS-210528.
- [13] Y. Yu, C. Li, B. Yang, Y. Zhang, and Z. Liu, "Suppressed circulating current of MMC with IPSO optimized PR controller," in *2020 Chinese Automation Congress (CAC)*, Nov. 2020, pp. 35–40. doi: 10.1109/CAC51589.2020.9326467.
- [14] L. Harnefors, A. Antonopoulos, K. Ilves, and H.-P. Nee, "Global asymptotic stability of current-controlled modular multilevel converters," *IEEE Transactions on Power Electronics*, vol. 30, no. 1, pp. 249–258, Jan. 2015, doi: 10.1109/TPEL.2014.2298560.
- [15] A. Antonopoulos, L. Angquist, L. Harnefors, K. Ilves, and H.-P. Nee, "Global asymptotic stability of modular multilevel converters," *IEEE Transactions on Industrial Electronics*, vol. 61, no. 2, pp. 603–612, Feb. 2014, doi: 10.1109/TIE.2013.2254100.
- [16] K. Sharifabadi, L. Harnefors, H. Nee, S. Norrga, and R. Teodorescu, *Design, control and application of modular multilevel converters for HVDC transmission systems*. Wiley, 2016. doi: 10.1002/9781118851555.
- [17] G. Zhang, J. Song, C. Li, and X. Gu, "A circulating current suppression strategy for MMC based on the 2N+1 PWM approach," *World Electric Vehicle Journal*, vol. 14, no. 4, Apr. 2023, doi: 10.3390/wevj14040106.
- [18] M. Moranchel, E. Bueno, I. Sanz, and F. Rodríguez, "New approaches to circulating current controllers for modular multilevel converters," *Energies*, vol. 10, no. 1, Jan. 2017, doi: 10.3390/en10010086.
- [19] W. Uddin, T. D. C. Busarello, K. Zeb, M. A. Khan, A. K. Yedluri, and H.-J. Kim, "Control strategy based on arm-level control for output and circulating current of MMC in stationary reference frame," *Energies*, vol. 14, no. 14, Jul. 2021, doi: 10.3390/en14144160.
- [20] G. Konstantinou, J. Pou, S. Ceballos, R. Picas, J. Zaragoza, and V. G. Agelidis, "Control of circulating currents in modular multilevel converters through redundant voltage levels," *IEEE Transactions on Power Electronics*, vol. 31, no. 11, pp. 7761–7769, Nov. 2016, doi: 10.1109/TPEL.2015.2512842.
- [21] R. Darus, J. Pou, G. Konstantinou, S. Ceballos, and V. G. Agelidis, "Controllers for eliminating the ac components in the circulating current of modular multilevel converters," *IET Power Electronics*, vol. 9, no. 1, pp. 1–8, Jan. 2016, doi: 10.1049/iet-pel.2014.0930.
- [22] S. Debnath, J. Qin, B. Bahrani, M. Saeedifard, and P. Barbosa, "Operation, control, and applications of the modular multilevel converter: A review," *IEEE Transactions on Power Electronics*, vol. 30, no. 1, pp. 37–53, Jan. 2015, doi: 10.1109/TPEL.2014.2309937.
- [23] F. Zhao, G. Xiao, M. Liu, and D. Yang, "A fast sorting strategy based on a two-way merge sort for balancing the capacitor voltages in modular multilevel converters," *Journal of Power Electronics*, vol. 17, no. 2, pp. 346–357, Mar. 2017, doi: 10.6113/JPE.2017.17.2.346.
- [24] S. Du, A. Dekka, B. Wu, and N. Zargari, "Passive cross-connected modular multilevel converters," in *Modular Multilevel Converters: Analysis, Control, and Applications*, Hoboken, NJ, USA: John Wiley & Sons, Inc., 2018, pp. 131–163. doi: 10.1002/9781119367291.ch5.
- [25] Z. Liu, W. Yu, H. Guo, W. Kong, C. Gan, and R. Qu, "A capacitor voltage sorting algorithm for modular multilevel converters (MMC) under low-frequency carrier modulation," in *2019 22nd International Conference on Electrical Machines and Systems (ICEMS)*, Aug. 2019, pp. 1–4. doi: 10.1109/ICEMS.2019.8922104.
- [26] G. Bergna-Diaz, A. Formentini, P. Zanchetta, and E. Tedeschi, "Particle swarm optimization tuning of modular multilevel converters in a time-invariant framework," in *2019 IEEE 13th International Conference on Power Electronics and Drive Systems (PEDS)*, Jul. 2019, pp. 1–8. doi: 10.1109/PEDS44367.2019.8998775.
- [27] C.-H. Liu and Y.-Y. Hsu, "Design of a self-tuning PI controller for a STATCOM using particle swarm optimization," *IEEE Transactions on Industrial Electronics*, vol. 57, no. 2, pp. 702–715, Feb. 2010, doi: 10.1109/TIE.2009.2028350.

BIOGRAPHIES OF AUTHORS



Mbarek Outazkrit     received the M.S degree in electrical engineering from Cadi Ayyad University in 2014. He also obtained the Agrégation degree in Electrical Engineering in 2016. He is a PhD student in Center of physics and engineering sciences in Hassan First University. His area of interest is modular multilevel converters MMC, power converter applications in power systems, grid integration of renewable energy sources. He can be contacted at email: m.outazkrit@uhp.ac.ma.



Faicel El aamri     received his PhD on PV systems from Hassan first University in 2018. He currently works as Professor at Hassan II University, Faculty of Sciences and technologies of Mohammedia, Morocco. His area of research interest is the control of Grid-connected PV inverters and power electronics. He can be contacted at email: f.elaamri@gmail.com.



Essaid Jaouide    was born in 27 January 1990 in Beni Mellal, Morocco. He is a PhD student in Laboratory of Radiation-Matter and Instrumentation (RMI), Faculty of Sciences and Technology, Hassan 1st University, Morocco. He received his master's degree in electrical engineering from Cadi Ayyad University Marrakech, in 2013. He also obtained the Agrégation degree in Electrical Engineering in 2018. His research is in fields impedance source power electronic converters and grid-connected photovoltaic systems. He can be contacted at email: e.jaouide@uhp.ac.ma.



Abdelhadi Radouane    was born in 1969. He received the Agregation degree in Electrical Engineering from the ENSET of Rabat, Morocco in 1996. In 2017, he obtained a Ph. D in Automatic Control. Since 2018, he joined the FST Settat, Hassan First University of Settat, Morocco as assistant-professor. He can be contacted at email: radouane.abdelhadi@gmail.com.



Azeddine Mouhsen    born in 10 July 1967, He is Professor of Physics at Hassan First University, Morocco, since 1996. He holds a PhD from Bordeaux I University (France) in 1995 and a thesis from Moulay Ismail University, Morocco, in 2001. He specializes in instrumentation and measurements, sensors, applied optics, energy transfer, radiation-matter interactions. He has taught courses in physical sensors, chemical sensors, instrumentation, systems technology, digital electronics and industrial data processing. He has published over 30 papers, and he is the co-inventor of one patent. Actually, he is the Director of Laboratory of Radiation-Matter and Instrumentation. He can be contacted at email: az.mouhsen@gmail.com.